

Characterization of iron oxide-silica nanocomposites in flames: Part II. Comparison of discrete-sectional model predictions to experimental data

Pratim Biswas^{a)} and Chang Yu Wu

*Aerosol and Air Quality Research Laboratory, Environmental Engineering and Science Division,
University of Cincinnati, Cincinnati, Ohio 45221-0071*

Michael R. Zachariah and Brian McMillin^{b)}

*Chemical Science and Technology Laboratory, National Institute of Standards and Technology,
Gaithersburg, Maryland 20899*

(Received 30 October 1995; accepted 6 September 1996)

A discrete-sectional model accounting for particle formation by chemical reaction and growth by coagulation and condensation is developed to predict the evolution of the nanocomposite aerosol size distribution in a multicomponent iron-silicon system in a flame. Particle formation by nucleation of the vapor is represented by an Arrhenius-type rate expression, with the rate constant being obtained from experiments and simulation results reported in the literature. Precursor vapor concentrations and the second aerosol volume moment predictions are compared to laser-induced fluorescence (LIF) and light scattering intensity measurements from experiments described in Part I²⁰ of the paper. The results elucidate the important formation and growth mechanisms of nanocomposite ferric oxide-silica particles in flame reactors. The role of operating parameters such as precursor characteristics and temperature profiles on the final product characteristics is established.

I. INTRODUCTION

Several physico-chemical processes are underway enroute to particle formation in multicomponent systems. To better understand the role of these different processes, it is important to model the behavior of such systems. The general dynamic equation (GDE), also called the population balance equation, is the governing equation that describes particle formation and growth.^{1,2} The GDE is a nonlinear, partial integro-differential equation, and several different approaches have been used to solve this equation to predict the evolution of the aerosol size distribution. Models that approximate the size distribution by a finite number of sections were developed by Gelbard and Seinfeld.³ The accuracy of these models depends on the selection of the integral property that is conserved and on the section spacing. To accurately predict the initial stages of particle formation, it is essential to use a discrete formulation.⁴⁻⁶ The computational time requirements of a complete discrete formulation are rather enormous, and the simulation is limited to a few milliseconds even on supercomputers.⁴ This led to the development of a discrete-sectional model,⁵ where a discrete representation is used for the smaller particles followed by a sectional representation of the larger sizes. Wu and Flagan⁵ used an

approximation similar to Gelbard *et al.*⁷ for the spacing of the sections, where a geometric approximation was made to simplify calculation of the coagulation kernels. Landgrebe and Pratsinis⁶ removed this restriction and used an arbitrary spacing of the sections.

In this paper, an approach similar to Landgrebe and Pratsinis⁶ is used to model the prediction of the aerosol size distribution. The discrete-sectional approach is extended to simulate particle formation and growth in multicomponent environments, and applied to a system for the formation of nanocomposite ferric oxide-silica particles. The model accounts for simultaneous chemical reaction to form the vapor phase precursor to particles, particle formation by a kinetic process, growth by coagulation, and condensation. The predictions of the model are compared to the results of experiments described in Part I.²⁰

II. MODEL DEVELOPMENT

The general dynamic equation for the gas to particle conversion process is^{1,2}

$$\begin{aligned} \frac{\partial n}{\partial t} + \frac{\partial(Gn)}{\partial v} - I'(v^*)\delta(v - v^*) \\ = \frac{1}{2} \int_0^v \beta(v - \tilde{v}, \tilde{v})n(v - \tilde{v}, t)n(\tilde{v}, t) d\tilde{v} - n(v, t) \\ \times \int_0^\infty \beta(v, \tilde{v})n(\tilde{v}, t) d\tilde{v} \end{aligned} \quad (1)$$

^{a)}Author to whom correspondence must be addressed.

^{b)}National Research Council/NIST Postdoctoral Fellow.

The first term on the left-hand side (LHS) is the rate of change of the particle distribution function in the particle volume interval v to $v + dv$, the second term on the LHS accounts for the effect of condensation at rate G , and the third term on the LHS describes the formation of new particles of critical volume v^* at rate I' . The terms on the right-hand side account for the effect of Brownian coagulation.

A schematic representation of the process occurring is shown in Fig. 1, with experimental details being described in Part I²⁰ of this paper. Iron carbonyl and hexamethyl disiloxane, individually and together, are introduced as precursors to a methane-oxygen-nitrogen flame. First, a discussion for a single precursor feed (Cases 1 to 5, Table II) is provided. The iron carbonyl vapors enter the flame region, decompose, and are oxidized to form iron oxide vapors. The formation of $\text{FeO}(\text{g})$ by oxidation of iron carbonyl is described by a first-order kinetic process (rate constant, $k_{1,\text{Fe}}$) in the presence of excess oxygen.⁸ Similarly, the oxidation of hexamethyl disiloxane is described by a first-order process in the presence of excess oxygen. As no data are available in the literature for oxidation rates of hexamethyl disiloxane, and as its decomposition to Si is rapid (see Fig. 1), the rate constant is assumed to be similar to that reported for silicon tetrachloride oxidation.⁹ These vapors then nucleate to form the oxide particles. Due to the low vapor pressures of the resultant oxides, classical descriptions^{1,2} of the nucleation phenomena indicate that there is no thermodynamic barrier to particle formation, and this clearly indicates that an atomistic approach needs to be used.¹⁰ Values of the rate constant, $k_{2,\text{Si}}$, for silica particle formation estimated by Zachariah and Tsang¹¹ are used in this work. Due to the complexities of the *ab initio* calculations for the rate constants, the second-order rate constant, $k_{2,\text{Fe}}$ (Fig. 1), for iron oxide particle formation was determined by fitting the

model simulation to the experimental results for one set of conditions (Case 2, Table II). Using a temperature dependency similar to that for silica particle formation, these were used to predict results for the other conditions (Cases 1 and 3). Particle growth occurs by coagulation and condensation. The expressions for the coagulation kernels are similar to those derived by Landgrebe and Pratsinis⁶ for an arbitrary section spacing, f_s . [The differences are the discrete-discrete collision integrals, Table IB, and the missing coefficient (misprint), $1/9$, in the $\ln^2 \sigma_g$ expression, Eq. B15, in the Landgrebe and Pratsinis paper.] The expressions for the condensation kernels are similar to the coagulation kernels, except that β is replaced by the free molecular condensation coefficient,¹ along with the Kelvin effect expression. Evaporation, however, is not considered. As mentioned earlier, a discrete-sectional representation is used to describe the aerosol, the lower sizes being represented by a discrete representation (volumes of sizes being multiples of molecular size of iron oxide and silica) followed by a sectional representation of spacing, f_s . The governing equations are written in the form of the ζ th aerosol volume moments, and are listed in Table I. For example, $\zeta = 0$ results in conservation of the total number, $\zeta = 1$ indicates conservation of total volume, and $\zeta = 2$ indicates conservation of the total volume squared. The choice of ζ has a physical connotation as to which integral property is conserved. The number of discrete sizes and sections are varied to ensure that the error is minimal.

When both components are introduced together into the flame region, an additional surface is available for condensation of iron oxide vapors, and the iron oxide and silica particles may also coagulate with each other. As discussed in Part I,²⁰ the precursor oxidation chemistries are independent and the oxidation rate constants are assumed to be the same as described earlier ($k_{1,\text{Fe}}$ and $k_{1,\text{Si}}$). Furthermore, for simplicity, it is assumed that there is no iron oxide particle and silica particle interaction in the discrete size ranges. Interaction by coagulation and condensation is accounted for particles in the sectional regimes, and is modeled similar to that by Gelbard and Seinfeld.¹² Also, as iron oxide and silica are not miscible, an accommodation factor, α , is used in the heterogeneous condensation expression. There are no reported values of α for iron oxide-silica systems in the literature, and hence the value is determined by fitting the predicted values to experimental measurements. The governing equations, in general form, are listed in Table I.

A summary of all the simulations performed is listed in Table II. Three classes of simulations were carried out: (a) iron precursor feed only (three different concentrations), (b) silicon precursor feed only (two concentrations), and (c) iron and silicon precursors fed

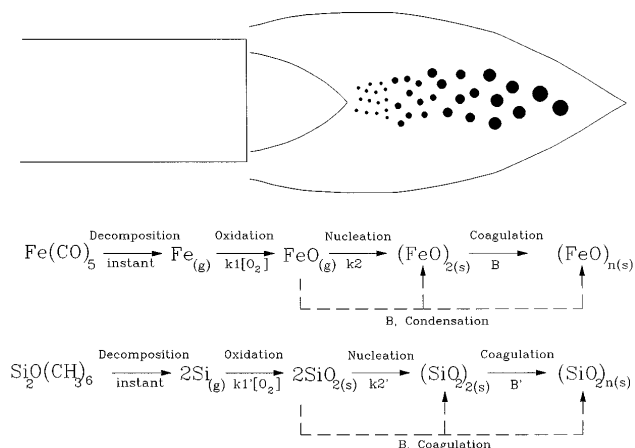


FIG. 1. Mechanisms of particle formation for the different feed conditions.

TABLE IA. The general dynamic equations for the multicomponent discrete-sectional model for the ζ th aerosol moment.

$\frac{dq_{2,m}}{dt} = k_{2,m}q_{1,m}^2 - q_{2,m} \sum_{j=2}^{\max_m} 2\overline{\beta}_{2,j,m}^{DD} q_{j,m} - q_{2,m} \sum_{k=1}^{\text{MAX}} 4\overline{\beta}_{2,k,m}^D Q_k - 4\overline{\beta}_{1,2,m}^{DD} (q_{1,m} - q_{2,\text{sat},m})q_{2,m}$	First discrete size
$\frac{dq_{i,m}}{dt} = \frac{1}{2} \sum_{j=2}^{i-2} 1\overline{\beta}_{j,i-j,m}^{DD} q_{j,m} q_{i-j,m} - q_{i,m} \sum_{j=2}^{\max_m} 2\overline{\beta}_{i,j,m}^{DD} q_{j,m} - q_{i,m} \sum_{k=1}^{\text{MAX}} 4\overline{\beta}_{i,k,m}^D Q_k - 4\overline{\beta}_{1,i,m}^{DD} (q_{1,m} - q_{i,\text{sat},m})q_{i,m} + 1\overline{\beta}_{i-1,i,m}^{DD} (q_{1,m} - q_{i-1,\text{sat},m})q_{i-1,m}$	Other discrete sizes
$\frac{dQ_1}{dt} = \frac{1}{2} \sum_{m=1}^{\max} \sum_{i=2}^{\max_m} \sum_{j=2}^{\max_m} 1\overline{\beta}_{i,j,1,m}^{DDS} q_{i,m} q_{j,m} - Q_1 \sum_{m=1}^{\max} \sum_{i=2}^{\max_m} 2\overline{\beta}_{i,1,m}^D q_{i,m} + Q_1 \sum_{m=1}^{\max} \sum_{i=2}^{\max_m} 5\overline{\beta}_{i,1,m}^D q_{i,m} - \frac{1}{2} 3\overline{\beta}_1 Q_1^2 + \frac{1}{2} 6\overline{\beta}_1 Q_1^2 - Q_1 \sum_{i=2}^{\text{MAX}} 4\overline{\beta}_{1,i} Q_i - \alpha \sum_{m=1}^{\max} 2\overline{\beta}_{1,1,m}^D (q_{1,m} - Q_{1,\text{sat},m})Q_1 + \alpha \sum_{m=1}^{\max} 5\overline{\beta}_{1,1,m}^D (q_{1,m} - Q_{1,\text{sat},m})Q_1 + \alpha \sum_{m=1}^{\max} 1\overline{\beta}_{1,\max,m,1}^{DDS} (q_{1,m} - q_{\max,\text{sat},m})q_{\max,m}$	First section
$\frac{dQ_k}{dt} = \frac{1}{2} \sum_{m=1}^{\max} \sum_{i=2}^{\max_m} \sum_{j=2}^{\max_m} 1\overline{\beta}_{i,j,k,m}^{DDS} q_{i,m} q_{j,m} - \sum_{m=1}^{\max} \sum_{i=2}^{\max_m} \sum_{j=2}^{k-1} 1\overline{\beta}_{i,j,k,m}^D q_{i,m} Q_j + \frac{1}{2} \sum_{i=1}^{k-1} \sum_{j=1}^{k-1} 1\overline{\beta}_{i,j,k} Q_i Q_j - Q_k \sum_{m=1}^{\max} \sum_{i=2}^{\max_m} 2\overline{\beta}_{i,k,m}^D q_{i,m} - Q_k \sum_{i=1}^{k-1} 2\overline{\beta}_{i,k} Q_i + Q_k \sum_{m=1}^{\max} \sum_{i=1}^{\max_m} 5\overline{\beta}_{i,k,m}^D q_{i,m} + Q_k \sum_{i=1}^{k-1} 5\overline{\beta}_{i,k} Q_i - \frac{1}{2} 3\overline{\beta}_k Q_k^2 + \frac{1}{2} 6\overline{\beta}_k Q_k^2 - Q_k \sum_{i=k+1}^{\text{MAX}} 2\overline{\beta}_{i,k} Q_i - 2\overline{\beta}_{1,k,m}^D \alpha Q_k (q_{1,m} - Q_{k,\text{sat},m}) + 5\overline{\beta}_{1,k,m}^D \alpha (q_{1,m} - Q_{k,\text{sat},m})Q_k + 1\overline{\beta}_{1,k-1,k,m}^D \alpha (q_{1,m} - Q_{k-1,\text{sat},m})Q_{k-1}$	Other sections
$\frac{dq_{1,m}}{dt} = k_{1,m} C_{\text{Pre},m} C_{\text{O}_2} (i v_{1,m})^\zeta - 2^{\zeta-1} k_{2,m} q_{1,m}^2 - \alpha \sum_{j=1}^{\max_m} 2\overline{\beta}_{1,j,m}^{DD} (q_{1,m} - q_{j,\text{sat},m})q_{j,m} - \alpha \sum_{k=1}^{\text{MAX}} 4\overline{\beta}_{1,k,m}^D (q_{1,m} - Q_{k,\text{sat},m})Q_k$	Precursor
$q_{1,m}$	Aerosol population function of vapor or the first discrete size of species m
$q_{i,m} = n_m(i v_1) \cdot (i v_1)^\zeta$	Aerosol population function of discrete size i of species m
$Q_k = N(v_k) \cdot (v_k)^\zeta$	Aerosol population function of section k
$q_{i,\text{sat},m} \left[= n_{\text{sat},m} \exp\left(\frac{4\sigma_m v_{1,m}}{k_B T d_{i,m}}\right) v_1^\zeta \right]$	Saturation aerosol population function of species m on the surface of discrete size i
$Q_{k,\text{sat}} \left[= n_{\text{sat},m} \exp\left(\frac{4\sigma v_{1,m}}{k_B T d_k}\right) v_1^\zeta \right]$	Saturation aerosol population function of species m on the surface of section k
m	Speciation variable
$v_{1,m}$	Volume of vapor or the first discrete size of species m
$n_m(i v_1)$	Number concentration of discrete size i
$N(v_k)$	Number concentration of section k
$n_{\text{sat},m}$	Saturation vapor number concentration of species m
ζ	Population index: 0-number, 1-volume, 2-volume square
$k_{1,m}$	Rate constant of vapor or first aerosol size formation from precursor of species m
$k_{2,m}$	Rate constant of nucleation from vapor or first aerosol size of species m
$C_{\text{Pre},m}$	Molar precursor concentration of species m
k_B	Boltzman constant
T	Temperature
σ_m	Bulk surface tension of species m
$d_{i,m}$	Aerosol diameter of discrete size i of species m
d_k	Aerosol diameter of section k
α	Accommodation factor for FeO
θ	Logical function: 0-false, 1-true
u, v	Aerosol volume variables
$\rho P, m$	Bulk density of species m

TABLE IB. Coagulation and condensation collision frequency functions for discrete-sectional model.

Discrete-Discrete	
${}^1\overline{\beta}_{i,j,i+j,m}^{DD} = \beta_m(iv_{1,m}, jv_{1,m}) \frac{[v_{1,m}(i+j)]^\zeta}{(iv_{1,m})^\zeta(jv_{1,m})^\zeta}$	$D_{i,m}$ with $D_{j,m}$ to form $D_{i+j,m}$
${}^1\overline{\beta}_{i,j,k,m}^{DDS} = \theta[v_{k-1} < v_{1,m}(i+j) < v_k] \beta_m(iv_{1,m}, jv_{1,m}) \frac{[v_{1,m}(i+j)]^\zeta}{(iv_{1,m})^\zeta(jv_{1,m})^\zeta}$	$D_{i,m}$ with $D_{j,m}$ to form S_k
${}^2\overline{\beta}_{i,j,m}^{DD} = \beta_m(iv_{1,m}, jv_{1,m}) / (iv_{1,m})^\zeta$	$D_{i,m}$ with $D_{j,m}$ to remove $D_{i,m}$
${}^4\overline{\beta}_{i,j,m}^{DD} = \beta_m(iv_{1,m}, jv_{1,m}) / (jv_{1,m})^\zeta$	$D_{i,m}$ with $D_{j,m}$ to remove $D_{j,m}$
Discrete-Section	
${}^1\overline{\beta}_{i,j,k,m}^D = \int_{v_{j-1}}^{v_j} \frac{\theta(v_{k-1} < iv_1 + u < v_k) (iv_1 + u)^\zeta \beta_m(u, iv_1)}{(iv_1)^\zeta u^\zeta (v_j - v_{j-1})} du$	$D_{i,m}$ with S_j to form S_k
${}^2\overline{\beta}_{i,k,m}^D = \int_{v_{k-1}}^{v_k} \frac{u^\zeta \beta_m(u, iv_1)}{(iv_1)^\zeta u^\zeta (v_k - v_{k-1})} du$	$D_{i,m}$ with S_k to remove S_k
${}^4\overline{\beta}_{i,k,m}^D = \int_{v_{k-1}}^{v_k} \frac{(iv_1)^\zeta \beta_m(u, iv_1)}{(iv_1)^\zeta u^\zeta (v_k - v_{k-1})} du$	$D_{i,m}$ with S_k to remove $D_{i,m}$
${}^5\overline{\beta}_{i,k,m}^D = \int_{v_{k-1}}^{v_k} \frac{\theta(iv_1 + u < v_k) (iv_1 + u)^\zeta \beta_m(u, iv_1)}{(iv_1)^\zeta u^\zeta (v_k - v_{k-1})} du$	$D_{i,m}$ with S_k to form S_k
Section-Section	
${}^1\overline{\beta}_{i,j,k} = \int_{v_{i-1}}^{v_i} \int_{v_{j-1}}^{v_j} \frac{\theta(v_{k-1} < u + v < v_k) (u + v)^\zeta \beta_k(u, v)}{u^\zeta v^\zeta (v_i - v_{i-1}) (v_j - v_{j-1})} du dv$	S_i with S_j to form S_k
${}^2\overline{\beta}_{i,k} = \int_{v_{i-1}}^{v_i} \int_{v_{k-1}}^{v_k} \frac{u^\zeta \beta_k(u, v)}{u^\zeta v^\zeta (v_i - v_{i-1}) (v_k - v_{k-1})} du dv$	Smaller S_i with S_k to remove S_k
${}^3\overline{\beta}_{i,k} = \int_{v_{k-1}}^{v_k} \int_{v_{k-1}}^{v_k} \frac{(u^\zeta + v^\zeta) \beta_k(u, v)}{u^\zeta v^\zeta (v_k - v_{k-1})^2} du dv$	S_k with S_k to remove S_k
${}^4\overline{\beta}_{i,k} = \int_{v_{i-1}}^{v_i} \int_{v_{k-1}}^{v_k} \frac{u^\zeta \beta_k(u, v)}{u^\zeta v^\zeta (v_i - v_{i-1}) (v_k - v_{k-1})} du dv$	Larger S_i with S_k to remove S_k
${}^5\overline{\beta}_{i,k} = \int_{v_{i-1}}^{v_i} \int_{v_{k-1}}^{v_k} \frac{\theta(u + v < v_k) (u + v)^\zeta \beta_k(u, v)}{u^\zeta v^\zeta (v_i - v_{i-1}) (v_k - v_{k-1})} du dv$	Smaller S_i with S_k to form S_k
${}^6\overline{\beta}_k = \int_{v_{k-1}}^{v_k} \int_{v_{k-1}}^{v_k} \frac{\theta(u + v < v_k) (u + v)^\zeta \beta_k(u, v)}{u^\zeta v^\zeta (v_k - v_{k-1})^2} du dv$	S_k with S_k to form S_k
Coagulation: $\beta_m(u, v) = \sqrt{\frac{6k_B Tr_{1,m}}{\rho_{P,m}}} \sqrt{\frac{1}{i} + \frac{1}{j}} \times (i^{1/3} + j^{1/3})^2$	
Condensation: $\beta_m(u, v) = \sqrt{\frac{6k_B Tr_{1,m}}{\rho_{P,m}}} i^{2/3}$	

together (one concentration of iron precursor and two concentrations of the silicon precursor). Along with the precursor feed conditions, the temperatures used in the simulations (as estimated by pyrometer measurements), the precursor decomposition rates, k_1 , the nucleation rates, k_2 , the oxygen concentrations, and the saturation pressure of FeO are listed. The sources and estimates of these parameter values are described in Sec. III. The predicted results are compared to the iron oxide vapor concentrations and light scattering intensities for the different cases. As the particles are primarily in the Rayleigh regime, it is anticipated that the light-scattering intensity will be proportional to volume square, and it was thus decided to choose $\zeta = 2$ for the simulations. However, to ensure that reasonable mass balances were being obtained, simulations for a specific condition

(case 2, Table II) were carried out with the values of $\zeta = 0, 1, \text{ and } 2$.

III. RESULTS AND DISCUSSION

Before a discussion of the comparison of model predictions to experimental results, two issues were considered. One was to determine the number of discrete sizes and section spacings, and the other was to check the mass balance error for simulations with $\zeta = 2$. The number of discrete sizes and section spacings were varied to ensure that the error was minimal. 40 discrete sizes were used for the iron oxide particles and 20 for the silica particles, followed by 52 sections. This resulted in a particle size range of approximately 0.3 nm to 300 nm. The percentage deviation (from the predictions

of chosen conserved variable) of the simulations for case 2 (Table II) with different values of ζ ($=0, 1, \text{ and } 2$) are shown in Table III for two sectional spacings, f_s of 1.42 and 1.25. The results indicate that if total number ($\zeta = 0$) was used as the conserved integral property, a significant mass balance error (15.5% deviation of total volume from the result of the simulation with total volume as the conserved variable for $f_s = 1.25$) would result. The error in the total volume squared is even higher (310%). If total mass is used as a conserved property, the error in total volume squared is about 72.5%. If volume squared ($\zeta = 2$) was chosen as the conserved property, the error in mass balance is about 1.08%. As the predictions of the model are to be compared to the light-scattering intensity (desirable to have a low error in total volume squared), $\zeta = 2$ was used for all the other simulations listed in Table II.

The temperature profiles measured using a radiation pyrometer are shown in Fig. 2. Though not the most accurate representation of the temperature profile in the flame, these provide for averaged measurements at

TABLE IIA. List of simulations performed.

Reactants	Flow rates (lpm @ 20 °C)	Mole fraction
Methane	0.93	0.11
Oxygen	2.33	0.28
Nitrogen	5.00	0.60
Argon (iron carbonyl bubbler)	0.05, 0.15, 0.24	
Argon (silicon bubbler)	0.14, 0.24	

Case no.	Precursor feed rates (10^{-6} moles/s)		LIF	Scattering
	Iron	Silicon		
1	1.06	...	x	x
2	3.09	...	x	x
3	5.10	...	x	x
4	...	3.47	...	x
5	...	5.73	...	x
6	3.09	3.47	x	x
7	3.09	5.73	x	x

TABLE IIB. List of parameter values.

Parameter	Value	Remarks
$k_{1,Fe}$	$1.5 \times 10^{12} \exp\left(-\frac{10060.14}{T}\right) \text{ cm}^3 \cdot \text{mole}^{-1} \cdot \text{s}^{-1}$	1/40 value reported in von Rosenberg and Wray ⁸
$k_{2,Fe}$	$10^{(5437.5/T+8.971)} \text{ cm}^3 \cdot \text{mole}^{-1} \cdot \text{s}^{-1}$	Interpolation from Zachariah and Tsang ¹⁰ and fitting to experimental data
$k_{1,Si}$	$4.86 \times 10^{17} \exp\left(-\frac{48288.67}{T}\right) \text{ cm}^3 \cdot \text{mole}^{-1} \cdot \text{s}^{-1}$	Powers ⁹
$k_{2,Si}$	$9.4 \times 10^{38} T^{-7.91} \exp\left(-\frac{12660}{2T}\right) + 2 \times 10^{23} T^{-3.06} \exp\left(-\frac{11470}{2T}\right) \text{ cm}^3 \cdot \text{mole}^{-1} \cdot \text{s}^{-1}$	Zachariah and Tsang ¹¹
$P_{\text{sat,FeO}}$	$10^{(-25169.5/T+9.6623)} \text{ mmHg}$	Equilibrium calculation ¹³
P_{2,SiO_2}	$10^{(-26428.4/T+13.43)} \text{ mmHg}$	CRC, 1994 ¹⁹

different distances from the flame front and were used in the simulations. The temperature remains approximately constant close to the flame front, and then decreases at downstream locations due to heat transfer to the surroundings. Due to the exothermic oxidation reaction of the iron carbonyl precursor, higher temperatures are measured at higher iron precursor feed rates. On addition of the silicon precursor, no appreciable temperature differences were observed.

In summary, on reviewing the equations in Table I, values of five parameters ($k_{1,Fe}$, $k_{2,Fe}$, $k_{1,Si}$, $k_{2,Si}$, and α) need to be established. $k_{1,Si}$ and $k_{2,Si}$ were obtained from the literature.^{9,11} Though $k_{1,Fe}$ is reported in the literature,⁸ the pre-exponent term was adjusted for better agreement with the measurements in this study (see discussion later). $k_{2,Fe}$ was obtained by comparing model predictions to experimental data in Case 2 and using a temperature dependence similar to that reported for silica particle formation.¹⁰ The value for α , the accommodation coefficient, was obtained by comparing the model predictions to Case 6. Equilibrium vapor pressures for the oxides were obtained as a function of temperature by using the results of an equilibrium program.¹³ Expressions for the parameters are listed in Table II. Simulations were carried out for the seven cases listed in Table II using these parameter values. The predictions were compared to experimental measurements [LIF for FeO(g) and light scattering] as listed in Table II.

A. Iron feed only

The predicted results of FeO(g) and the measured FeO(g) concentrations along the centerline of the flame for the “iron only” feed conditions are shown in Fig. 3. The pre-exponent in the $k_{1,Fe}$ expression was reduced to 1/40th the value reported by von Rosenberg and Wray⁸ for better agreement with data in all the simulations. A possible explanation for this could be the use of a higher temperature in the simulations close to the flame front, resulting in an underprediction of the time. Rather

TABLE III. List of percentage deviation for different conserved variable.

Conserved variable	Deviation (%)		
	Particle number (#/cm ³)	Element mass (mol/cm ³)	Particle volume ² (cm ⁶ /cc)
$f_s = 1.42$			
Particle number	0	31.7	503.8
Particle volume	35.7	0	83.6
Particle volume ²	28.3	1.55	0
$f_s = 1.25$			
Particle number	0	15.5	310.3
Particle volume	28.8	0	72.5
Particle volume ²	24.7	1.08	0

than alter the temperature profile (Fig. 2), it was decided to lower the pre-exponent term in the rate expression and good agreement was obtained in all cases (1, 2, 3, 6, and 7). Case 2 was used as a base condition to determine the nucleation rate constant, $k_{2,Fe}$ by fitting model predictions to the measured data. The temperature dependence of the nucleation rate constant was assumed to be similar to that of silica particle formation.¹⁰ As seen in Fig. 3, good agreement is obtained between the predicted FeO(g) concentrations and measured values for all three cases. Iron carbonyl decomposes and is oxidized to form FeO(g), resulting in an increase in FeO(g) concentration at initial times. As the FeO(g) concentration builds up, particle formation is initiated (modeled by a second-order rate process), resulting in the decrease in FeO(g). Particle growth at initial times occurs by Brownian coagulation. The newly formed iron oxide particles also act as a sink for FeO(g) by condensation, and this mode of particle growth is more dominant at later times (greater than about 3 cm, where the temperature also begins to drop). At initial times

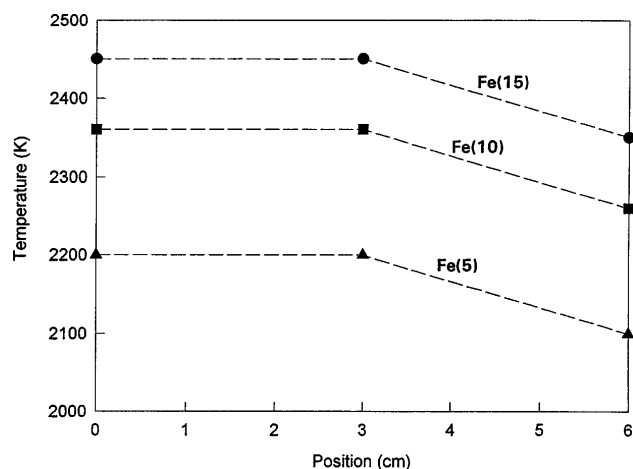


FIG. 2. Temperature profiles for the different experiments as measured by ratio pyrometry.

condensation is not important due to higher temperatures and the presence of small particles (Kelvin effect).

Figure 4 is a comparison of the measured light scattering intensity to the predicted second volume moment of the aerosol size distribution for the “iron only” feed conditions. The particles formed are in the nanometer size ranges and in the Rayleigh regime, and therefore the light scattering intensity should be proportional to the second volume moment. Case 2 was again used as a base condition to obtain the optical system parameters by scaling the measured data to predicted values of the second volume moment. The scattering intensity for Case 1 is very small, as is predicted by the model. The simulation result for Case 3 is slightly lower than the measured scattering intensities, especially at later times. At higher feed rates of iron carbonyl, flicker due to buoyancy driven shear layers was observed at the outer edge of the flame, and this could carry particles from the outer peripheries (larger due to enhanced growth in the cooler

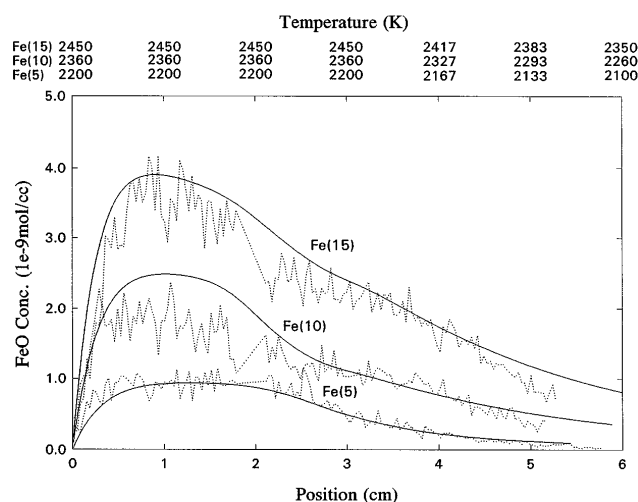


FIG. 3. Predicted centerline profile of FeO(g) concentration as a function of distance from the flame front for three different iron precursor feed rates (Cases 1, 2, and 3). The dashed lines represent experimental data.

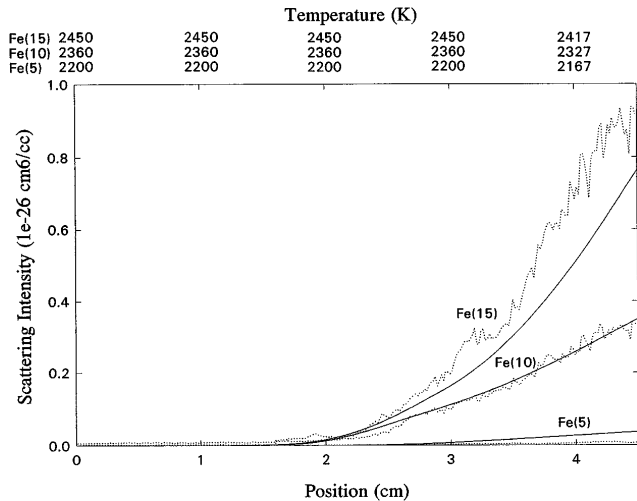


FIG. 4. Comparison of the second aerosol volume moment to measured scattering intensities along the centerline for the three different iron precursor feed rates. Dashed lines represent measured data scaled by matching Case 2 to the predicted results.

regions) to the centerline, and result in higher measured average (averaged typically over 250 measurements in five minutes) intensities. The lower predicted values may also be due to the assumption of ideal sintering (perfect spheres). Though the sintering rates for iron oxide are high, this assumption is nonetheless violated. It must be noted that this difference is rather insignificant as the ratio of the measured to predicted intensity is about 1.2 at 4 cm, which would result if there was a deviation of only 3% in the particle diameter.

B. Co-feed of iron and silicon precursor

The simulation results for a co-feed of the iron and silicon precursor (Cases 2, 6, and 7) are shown in Fig. 5,

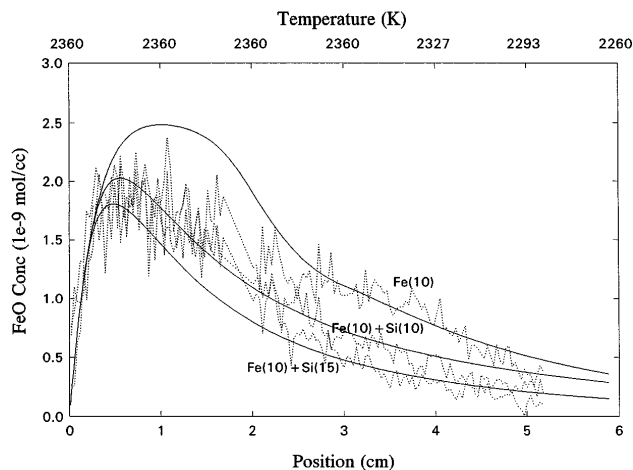


FIG. 5. Predicted centerline profile of FeO(g) concentration as a function of distance from the flame front for the iron precursor feed condition (Case 2) and iron and silicon feed conditions (Cases 6 and 7). The dashed lines represent experimental data.

and compared to the centerline measured FeO(g) concentrations. Due to the presence of silica particles in addition to the iron oxide particles, condensation occurs on a heterogeneous surface [FeO(g) condensing onto a silica particle]. On examining the morphology of the particles, one finds that the iron oxide particles are embedded in a silica matrix, with the iron oxide particles close to the surface. The iron oxide and silica particles appear to be immiscible; thus, the condensation rate was lowered by a factor, similar to an accommodation coefficient, α , described by Friedlander.¹ Values for α were determined by comparison to the experimental measurements (≈ 0.025) for Case 6. Good agreement is obtained for the multiple precursor simulations (Cases 6 and 7) with experimental data. At initial times, there is no difference in the predicted FeO(g) concentrations for Cases 2, 6, and 7 when the concentration is increasing. This is due to the assumed independent precursor decomposition chemistry which is consistent with the observations. Further downstream (distance greater than approximately 2 cm) the measured FeO(g) concentration decreases more rapidly in the experiments with the silicon precursor co-feed (Cases 6 and 7) and in comparison to Case 2. The predicted decrease, however, occurs at earlier time instants, and this is due to the predicted enhanced calculated condensation of FeO(g) onto the surface of the silica particles.

The measured light scattering intensities for Cases 2, 4, 5, 6, and 7 are compared to the predicted values in Fig. 6. The optical system parameter used for the iron oxide measurements was used to scale the co-feed scattering data, with a correction for the refractive index ratio for silica particles to iron oxide particles (as the outer shell is predominantly silica). The ratio of the refractive index of silica to iron oxide is approximately

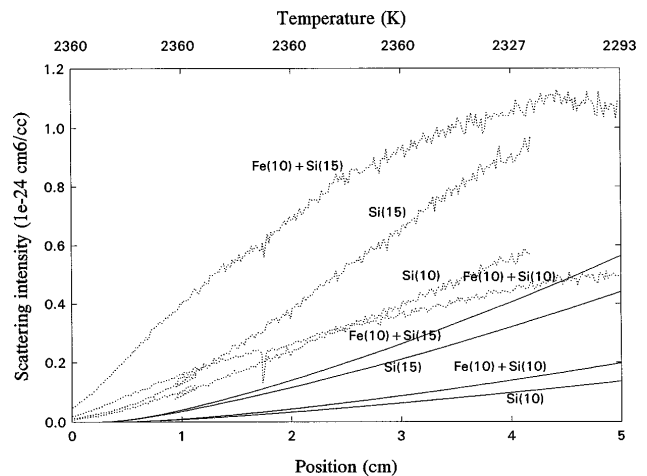


FIG. 6. Comparison of the second aerosol volume moment to measured scattering intensities along the centerline for the silicon only (Cases 4 and 5) and iron and silicon feed (Cases 6 and 7) experiments. The dashed lines represent measured data.

1 : 2 (CRC, 1994).¹⁹ The measured scattering intensities are all greater than the predicted values. This is because of the assumption of infinitely fast sintering rates in the simulations. The sintering rates for silica are not as high as iron oxide, resulting in sintering time constants of the same order as the measurement time scales.¹⁴ As sintering of the silica particles is not complete, the scattering cross sections are much larger than that of a spherical particle, and the measured intensities are higher than the predicted values, similar to that reported by Zachariah *et al.*¹⁵ The experimental results for the silicon precursor only (Cases 4 and 5) provide interesting comparisons to the results for the co-feed precursors (Cases 6 and 7). At initial times, the scattering intensity for the co-feed cases (6 and 7) exceeds that of the corresponding “silicon feed only” (Cases 4 and 5) experiments, as is expected and also predicted by the model. However, at further distances downstream, the scattering intensity for the silicon-only experiment exceeds the co-feed case (Case 4 compared to Case 6), and a similar trend is observed for the results of Cases 5 and 7. The presence of the iron oxide in the silica particle enhances the sintering rate of the composite particles, probably due to the lower melting point and higher surface tension of iron oxide relative to silica. Sintering thus results in the coalescence into closer to spherical shapes, and results in flattening the scattering intensity profiles, a similar behavior being observed by Hung and Katz¹⁶ in their light-scattering experiments. A similar behavior was observed for germania-silica systems by Chang *et al.*¹⁷

C. Implications

The model can be used to relate the processing conditions to resultant particle characteristics. Several parameters affect the final product characteristics, and these include the temperature, residence time, precursor characteristics, and feed rates. The temperature can be controlled by adjusting the fuel to air ratio, and it affects the precursor decomposition and particle formation rates. Varying the residence time results in different particle sizes and provides guidelines for the design of the collection system (see Part I). The precursor feed rates also affect the various dynamic mechanisms that establish the resultant particle size distribution. A number of simulations were carried out by varying the different parameters to 0.1 and 10 times the base value (Case 6, Table IIA). The FeO(g) concentration and light-scattering intensity as a function of position (distance from the flame front) is plotted in Fig. 7 for different simulation conditions. The mean particle size, standard deviation, and number concentration of particles relative to the base case simulation are listed in Table IV.

The use of different precursors would alter the rate of formation of FeO and subsequently the iron oxide particles. The rate constant, $k_{1,Fe}$, was increased to 10 times and reduced to 0.1 times the base value listed in Table IIB. On increasing the rate constant (precursor that decomposes rapidly), not much change is observed in the mean diameter, standard deviation, or total number concentration (Table IV). This is because the current precursor being used has a high decomposition rate, and further increases do not result in any changes in the resultant particle size distributions. For precursors with a slower decomposition rate (Case 2, Table IV), the iron oxide vapors and subsequently the particles are formed at later stages, resulting in a larger number concentration (1.77 times the base case) of smaller sized particles (0.77 times the base case). Varying the precursor rate (Cases 3 and 4) does not affect the resultant particle size significantly; however, the total mass of particles is proportional to the feed rate, and this is reflected in the resulting total number of concentrations. For higher feed rates, the resultant temperatures are higher (see Fig. 2) and this suppresses condensational growth. For lower feed rates though, the temperatures are lower (Fig. 2, enhancing condensational growth), and the growth by coagulation is diminished. The temperature history in the flame region is a sensitive parameter that affects the aerosol size distribution significantly. On increasing the temperature (Case 5) by 100 K, the condensation mode of growth is significantly suppressed, and the resulting particles are smaller. As the feed rate is the same, this results in a higher total number concentration. The opposite effect is observed on reducing the temperature (Case 6). Condensational growth is enhanced and results in a smaller number of larger particles. The silicon precursor decomposition rate has a similar dependence as the iron precursor. Further increase in the decomposition rate does not affect resultant particle characteristics as the existing precursor decomposition is rather rapid. On choosing a slower decomposition rate, a larger number concentration of smaller particles are obtained. Increasing the silicon precursor feed rate (Case 9) provides more surface area for condensational growth, resulting in large size particles.

In addition, two sensitive parameters that affect the resultant particle characteristics are the iron oxide nucleation rate, k_2 , and the accommodation factor, α . Calculations using the classical theory of nucleation for many oxides indicate that there is no thermodynamic barrier to nucleation, and therefore one must use an atomistic approach.¹⁰ One simplification made by several researchers is that the monomer is a stable particle, especially for many oxide systems.^{6,18} Assuming that the monomer is a stable particle in this system results in erroneous predictions [Fig. 7(b)] of both FeO(g) concentrations and the light-scattering intensities (as compared

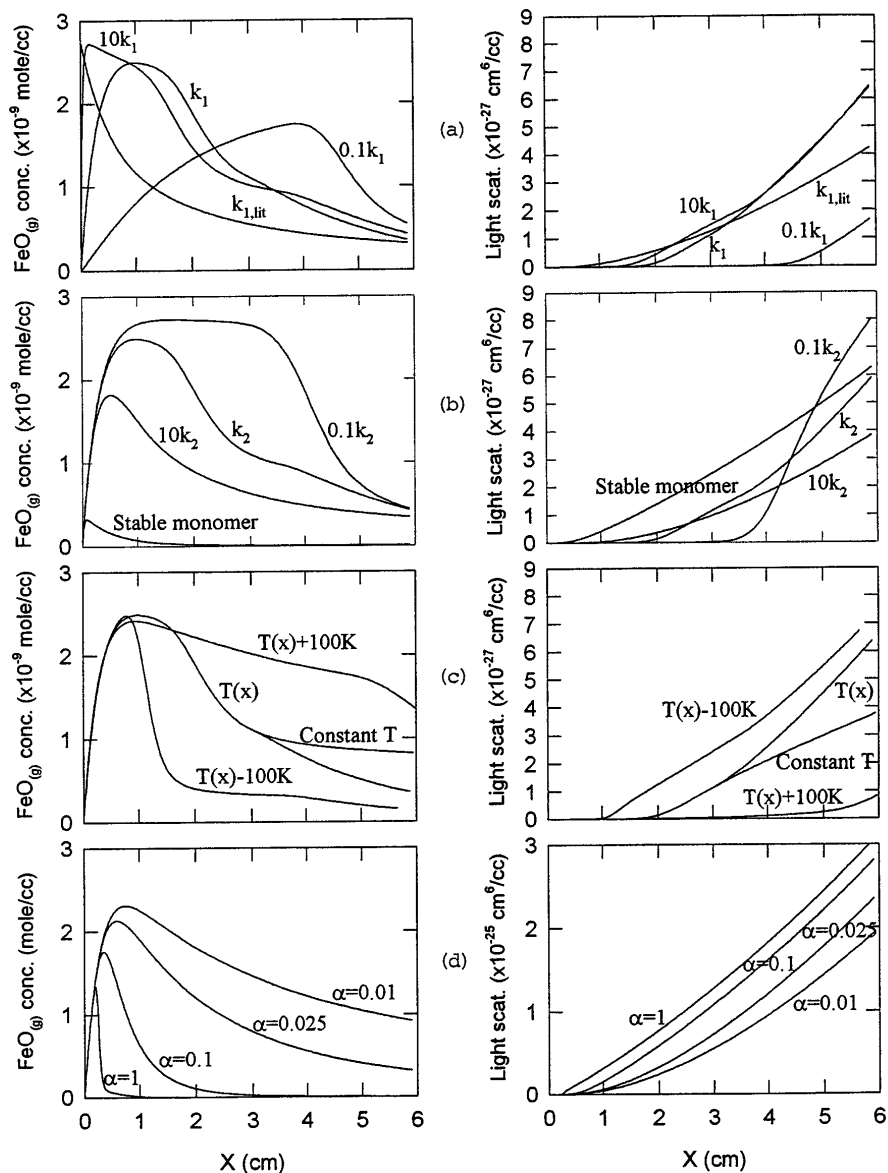


FIG. 7. Sensitivity analysis of FeO(g) concentrations and light-scattering intensities for variation of (a) iron precursor oxidation rate, k_1 , (b) iron oxide nucleation rate, k_2 , (c) temperature history, $T(x)$, and (d) accommodation factor, α .

to estimated data, Figs. 3 and 4). This indicates that nucleation is an important phenomenon, and one has to use an atomistic approach to describe it. To examine the effect of the nucleation rate (k_2), it was varied and the results are shown in Fig. 7(b). For a lower value of k_2 (relative to the base case), the FeO(g) concentration decreases at a slower rate and the particle formation is delayed as observed in the variation of the light-scattering intensity. The opposite effect is observed for higher values of k_2 .

Another sensitive parameter is the accommodation factor, especially for composite systems. The base case value of α was 0.025, which is the fraction of FeO molecules sticking to the composite FeO–SiO₂ particle

on impingement. Higher values of α result in faster growth rates of particles [as indicated by the increase in the light-scattering intensity, Fig. 7(d)] and faster decrease in FeO(g) concentrations.

IV. SUMMARY AND CONCLUSIONS

A discrete sectional model to predict the evolution of the aerosol size distribution during the formation of nanocomposite particles in flames was developed. The model accounted for precursor oxidation, particle formation, and growth by coagulation and condensation. Simulations were performed for a system consisting of an iron and silicon precursor, and the predicted results were

TABLE IV. Variation of mean particle size, geometric standard deviation, and total number concentration relative to the base case (Case 6, Table IIA) for different parameter values.

Case no.	Parameter	Range	Ratio		
			$d_{pv}/d_{pv,base}$	$\sigma_g/\sigma_{g,base}$	N/N_{base}
1	$k_{1,Fe}$	10 $k_{1,base}$	1.0030	0.9935	0.9913
2		0.1 $k_{1,base}$	0.7655	0.8845	1.7776
3	Fe feedrate	Fe(15)	0.9194	0.8646	1.9499
4		Fe(5)	0.8072	0.7753	0.7220
5	Temperature	+100 K	0.449	0.621	6.3365
6		-100 K	1.342	0.9404	0.4603
7	$k_{1,Si}$	10 $k_{1,base}$	1.0150	1.0107	0.9559
8		0.1 $k_{1,base}$	0.6860	0.6880	2.9760
9	Si feedrate	Fe(10) + Si(15)	1.2567	1.0826	0.7888

compared to laser-induced fluorescence measurements of vapor phase iron oxide and light scattering intensity measurements of the particles. After establishing the unknown parameter values by comparison to base case experiments, good agreement was obtained for the other experiments. The model helped elucidate the important mechanisms of particle formation and growth of iron oxide-silica nanocomposites. It can be used as a design tool for choosing operating conditions and precursors to obtain desired resultant particle characteristics.

REFERENCES

1. S. K. Friedlander, *Smoke, Dust and Haze* (John Wiley and Sons, New York, 1977).
2. J. H. Seinfeld, *Atmospheric Chemistry and Physics of Air Pollution* (Wiley Interscience, New York, 1986).
3. F. Gelbard and J. H. Seinfeld, *J. Comp. Phys.* **28**, 357 (1978).
4. M. Frenklach and S. J. Harris, *J. Colloid Int. Sci.* **118**, 252 (1987).
5. J. J. Wu and R. C. Flagan, *J. Appl. Phys.* **61**, 1365 (1988).
6. J. D. Landgrebe and S. E. Pratsinis, *J. Colloid Int. Sci.* **139**, 63 (1990).
7. F. Gelbard, Y. Tambour, and J. H. Seinfeld, *J. Colloid Int. Sci.* **76**, 541 (1980).
8. C. W. von Rosenberg and K. L. Wray, *J. Quant. Spectrosc. Radiat. Transfer* **12**, 531 (1972).
9. D. R. Powers, *J. Am. Ceram. Soc.* **61**, 295 (1978).
10. M. R. Zachariah and W. Tsang, *Aerosol Sci. Technol.* **19**, 499 (1993).
11. M. R. Zachariah and W. Tsang, *J. Phys. Chem.* **99**, 5308 (1995).
12. F. Gelbard and J. H. Seinfeld, *J. Colloid Int. Sci.* **78**, 485 (1980).
13. C. Y. Wu and P. Biswas, *Comb. Flame* **93**, 31 (1993).
14. G. D. Ulrich and J. W. Riehl, *J. Colloid Int. Sci.* **87** (1), 257 (1982).
15. M. R. Zachariah, D. Chin, H. G. Semerjian, and J. L. Katz, *Comb. Flame* **78**, 287 (1989).
16. C. H. Hung and J. L. Katz, *J. Mater. Res.* **7**, 1861 (1992).
17. H. Chang, W. Y. Lin, and P. Biswas, *Aerosol Sci. Technol.* **22**, 24 (1995).
18. P. Biswas, X. Li, and S. E. Pratsinis, *J. Appl. Phys.* **65**, 2445 (1989).
19. *CRC Handbook of Chemistry and Physics*, 75th ed. (CRC Press, Boca Raton, FL, 1994).
20. B. K. McMillin, P. Biswas, and M. R. Zachariah, *J. Mater. Res.* **11**, 1552 (1996).